PCCP

ROYAL SOCIETY OF CHEMISTRY

PAPER

View Article Online
View Journal | View Issue

Cite this: *Phys. Chem. Chem. Phys.*, 2021, **23**, 17672

Comparison of the heat-treatment effect on carrier dynamics in TiO_2 thin films deposited by different methods†

Ramsha Khan, [a] Harri Ali-Löytty, [b] Antti Tukiainen[c] and Nikolai V. Tkachenko *[a]

Polycrystalline titanium dioxide thin films are routinely used in a broad range of applications where charge carrier lifetime is essential for their performance but the effects of the fabrication method are rarely considered. Here we compare three popular deposition methods, atomic layer deposition (ALD), ion beam sputtering (IBS), and spray pyrolysis deposition (SPD). In all three cases, 30 nm thin films of TiO_2 are prepared, and the as-deposited films show no defined crystal structure and can be classified as amorphous films. Heat treatment (HT) of the films converts all of them to polycrystalline anatase TiO_2 as revealed by XRD measurements. A photophysical study was carried out by pico- to nano-second transient absorption pump–probe spectroscopy in transmittance and reflectance modes which allows taking into account the effects due to the photoinduced refractive index changes. This study shows that the HT increases the lifetime of the photo-carriers gradually to a nanosecond time domain (approx. 4 ns) as compared to a few picoseconds of the as-deposited samples. The photo-carrier dynamics of the samples become very similar after heat-treatment, though the topographical features and texture of the films observed with AFM and XRD are quite different. The measured transient absorption spectra of the samples also indicate that the photo-carrier relaxation pathway involves electron and hole trap states with the longest-lived being the hole traps. To evaluate the photoactivity of thin films, methylene blue (MB) photodegradation was tested for all the as-deposited and HT samples and the results showed a 20% higher degradation rate for the IBS HT sample due to the more textured surface.

Received 16th June 2021,
Accepted 22nd July 2021

DOI: 10.1039/d1cp02716f

rsc.li/pccp

1 Introduction

Interest in TiO_2 has arisen since it shows applications in water splitting,[1,2] photo-degradation[3–5] and as a photoanode in photovoltaic cells.[6,7] TiO_2 has been considered an important semiconductor metal oxide (MO) because it is often used as a photocatalyst for its low cost, non-toxicity and high chemical stability.[8] Anatase and rutile are the most common crystalline forms of TiO_2 and they both show different photocatalytic activities under light irradiation. The band gap of anatase TiO_2 is 3.2 eV while that of rutile TiO_2 is 3.0 eV.[9] TiO_2 in its anatase phase shows better photocatalytic performance than in its rutile phase for most applications due to its higher reduction potential.[10]

The lifetime of photogenerated charge carriers is one of the important factors determining the photocatalytic efficiency of semiconductor MO.[11] The photoexcitation generates instantly electron–hole pairs in the semiconductor. Then, the carriers either recombine, get trapped in the meta-stable states or they travel to the surface to undergo interfacial charge transfer for reacting with the adsorbed species.[12] One of the problems with semiconductor photocatalysts is the recombination of these photogenerated electron–hole pairs within a few ps[13] which hampers the efficiency of photocatalytic processes. Exploiting the charge carrier dynamics is thus crucial for understanding the photocatalytic mechanism and increasing the lifetime of the charge carriers for improved performance in photocatalytic applications.

The recombination of electron–hole pairs occurs in the bulk or surface defect states.[14,15] Kong *et al.*[15] have shown that decreasing the ratio of bulk holes to surface holes improves the efficiency of photocatalytic reactions. Formation of TiO_2

[a] *Photonic Compounds and Nanomaterials Group, Faculty of Engineering and Natural Sciences, Tampere University, P.O. Box 692, 33014 Tampere, Finland. E-mail: nikolai.tkachenko@tuni.fi; Tel: +358 40 7484160*
[b] *Surface Science Group, Faculty of Engineering and Natural Sciences, Tampere University, P.O. Box 692, 33014 Tampere, Finland*
[c] *Faculty of Engineering and Natural Sciences, Tampere University, P.O. Box 692, 33014 Tampere, Finland*

† Electronic supplementary information (ESI) available: The modelling for steady state absorbance spectra, estimation of photoinduced absorbance change by transient absorption measurements, their interpretations and the distributed decay model for lifetime calculation of thin films. See DOI: 10.1039/d1cp02716f

thin films by different deposition methods leads to the formation of films with different intrinsic defect states which directly affect the lifetime of charge carriers. The electronic properties of TiO_2 depend strongly on the defect disorders in the crystal lattice. The knowledge of defect states is essential for achieving the long lifetime of charge carriers for photocatalytic applications. Shallow trap states increase the diffusion distance of charge carriers hence promoting reactivity, while deep trap states enhance the recombination of charge carriers, hence making them unable to participate in chemical reactions.[16] However, oxygen vacancies act as both shallow and deep trap states. Also, electron trapping decreases the mobility of electrons and increases the lifetime of holes.

Transient absorption spectroscopy (TAS) is an effective technique to study the photodynamics of semiconductors.[13] It provides information about photogenerated charge carriers as they exhibit characteristic absorption features in the visible and infrared (IR) regions. The TAS study of TiO_2 yields knowledge about free and shallow trapped electrons as they exhibit structureless broad absorption with high intensity in the IR wavelength range.[17] On the other hand, deep trapped electrons have absorption in the visible and near-infrared (NIR) regions, which is explained by the transition of electrons from mid-gap states to the conduction band (CB).[18] By the TAS method, one can compare the dynamics of electrons and holes in TiO_2 thin films and elucidate the trap states which play an essential role in minimizing the charge carrier recombination by increasing their lifetime and hence in enhancing the photocatalytic efficiency.

Herein, we report on three deposition techniques, namely atomic layer deposition (ALD), ion beam sputtering (IBS) and spray pyrolysis deposition (SPD), employed to deposit TiO_2 thin films, which were post-processed and studied to identify the best technique providing the longest charge carrier lifetime. The targeted thickness of all films was 30 nm, which were deposited on quartz substrates. The films were studied after deposition, as-deposited (as-dep.), and after heat-treatment at 500 °C (HT) which induced crystallization of amorphous as-deposited TiO_2 to anatase TiO_2. The electron and hole trap states and comparison of charge carrier dynamics of TiO_2 thin films prepared by all these techniques have not been studied before to the best of our knowledge. Therefore, this study provides information on choosing an optimum thin film fabrication method for photocatalytic applications. Our results show that in terms of charge carrier dynamics, all the considered fabrication methods provide equally good carrier lifetimes with crystallization after heat-treatment. However, the thin film morphologies are different and must be critically considered in applications, where TiO_2 thin films serve as a protective or anti-reflective coating.

2 Experimental section

2.1 Film deposition

All samples were deposited on 1 mm thick UV-quality quartz substrates ($T > 80\%$ at 185 nm, Präzisions Glas & Optik GmbH).

2.1.1 Atomic layer deposition (ALD). ALD deposition of TiO_2 was carried out using a Picosun Sunale ALD R200 Advanced reactor. Tetrakis(dimethylamido) titanium(IV) ($Ti(N(CH_3)_2)_4$, TDMAT, electronic grade 99.999+%, (Sigma-Aldrich, Inc.), ultrapure Milli-Q water, and Ar (99.9999%, Oy AGA Ab, Finland) were used as the Ti precursor, O precursor, and carrier/purge/venting gas, respectively. During the ALD, the substrate temperature was kept at 150 °C. The film growth rate was calibrated by ellipsometry (Rudolph Auto EL III Ellipsometer, Rudolph Research Analytical). A TiO_2 film with a thickness of 30 nm (636 ALD cycles) was used for all the experiments. The precursors for ALD TiO_2 and a growth temperature of 150 °C were chosen based on the previous studies.[19,20]

2.1.2 Ion beam sputtering (IBS). Ion-beam sputtered (IBS) TiO_2 films were grown using a CEC Navigator 700 deposition system (Cutting Edge Coatings GmbH). Sputtering was performed under a reactive O_2 atmosphere (4.5×10^{-4} mbar) using an Ar/O_2 gas mixture (8 sccm/5 sccm) as the process gas and a Ti plate (99.8%) as the target. The sputtering voltage was 2 kV and the RF power of the ion source was 148 W. During the deposition, the sample holder was rotated at 60 rpm to guarantee uniform deposition. TiO_2 films of 30 nm thickness were prepared and the thickness was controlled *via in situ* broadband optical monitoring. The average growth rate for TiO_2 was 0.085 nm s^{-1}.

2.1.3 Spray pyrolysis deposition (SPD). TiO_2 was deposited over quartz substrates by a spray pyrolysis method. A clean quartz plate was placed on a heating plate at 200 °C. A solution of titanium di-isoproxide bis(acetylacetone) (Aldrich) in 2-propanol was prepared and sprayed onto the quartz substrate for 5 s with 0.12 MPa nitrogen gas to keep the atmosphere inert.[21] The coating was repeated after 1 minute. 64 cycles of spraying were carried out to obtain the desired thickness of close to 30 nm.

2.1.4 Post-treatment of as-deposited samples. Heat-treatment (HT) was performed in a tube furnace (Carbolite MTF 12/38/400 equipped with a quartz work tube) in air at 500 °C for 1 h using 10 °C min^{-1} for heating and cooling ramp rates.

2.2 Methods

2.2.1 AFM. To assess the grain boundaries and structure of the prepared as-deposited and heat-treated thin films, atomic force microscopy (AFM) was used in tapping mode (Veeco dimensions 2100).

2.2.2 XRD. Grazing incidence X-ray diffraction (GIXRD, Panalytical X'Pert^3 PRO and Panalytical Empyrean diffractometers, Malvern Panalytical Ltd, Malvern, UK) was performed to analyze the crystalline phase of both as-deposited and heat-treated TiO_2 thin films deposited *via* ALD, IBS and SPD methods. The samples were analyzed with Cu Kα radiation ($\lambda = 1.5405$ Å, $h\nu = 8.04$ keV) using 45 kV and 40 mA as the cathode voltage and current, respectively. The samples were scanned in 2θ between 20° and 55° with a grazing angle of 0.3° for the X-rays.

2.2.3 Absorption spectroscopy. Steady state absorption spectra were recorded from a Shimadzu UV-3600 UV-Vis-NIR spectrophotometer in both transmittance and reflectance

modes in the range of 250–1200 nm. For measuring the steady state reflectance, a 'Specular Reflectance Attachment for 5° Incidence Angle' accessory was used. Aluminium coated mirrors were used for reference. Ultrafast time resolved absorption spectroscopy was performed using a transient absorption pump–probe instrument described elsewhere.[22] In brief, the fundamental laser pulses were generated by a Ti:Sapphire laser (Libra F, Coherent Inc., 800 nm, ≈100 fs pulse width, repetition rate of 1 kHz). Most of the fundamental beam was directed to the optical parametric amplifier (Topas C, Light Conversion Ltd) to produce the excitation wavelength of 320 nm with an energy density of roughly 100 μJ cm^{-2}. The measurement system (ExciPro, CDP system) was equipped with two pairs of array detectors, Si CCD for visible and InGaAs for IR spectra detection. The measured signals were the average of two scans by averaging 2000 shots at each delay time. Measurements were acquired by detecting the transmitted probe (transmittance mode) and reflected probe (reflectance mode) from one and the same sample spot and the same excitation density in two wavelength ranges consecutively.

2.2.4 Methylene blue degradation test. TiO_2 films on quartz substrates were placed in a quartz cuvette (type: 3/Q/50, path length 50 mm, nominal volume 17.5 ml, Starna Scientific Ltd.) filled with 15 ml of 1.5 ppm methylene blue (MB) aqueous solution (diluted from 319112 0.05 wt% MB, Sigma-Aldrich) in the dark for 30 min to allow the MB to adsorb onto the film surface. The photodegradation of MB was initiated and conducted under UV light irradiation (300–400 nm, optical power of 20 mW cm^{-2}) using a filtered Xe-lamp as the light source (MAX-350 equipped with a UV-Vis mirror module (300–600 nm), a quartz light guide (1 m), a collimator lens (×1.0 RLQL80-1), and a shortpass filter/UV 400 nm (XHS0400), Asahi Spectra Co., Ltd) under convection induced by a magnetic stirrer (cuvetteMIXdrive 1, 2 mag AG). The film area exposed to UV light was 3.75 cm^2. The optical power was measured using a thermal power sensor (S401C, Thorlabs, Inc.). The MB concentration was measured online by monitoring the transmission, T, of a 635 nm laser beam (CPS635R Collimated Laser Diode Module and Mounted Si Photodiode SM1PD1A, Thorlabs, Inc.) through the cuvette. The concentration of MB is linearly proportional to the absorbance, $-\log(T)$, at 635 nm. The excitation spectrum, MB absorbance and the MB calibration curve are presented in Fig. S13 (ESI†).

3 Results

3.1 Steady state absorbance

The absorbance spectra were calculated from the measured reflectance R and transmittance T steady state spectra using eqn (1). The details of calculations are provided in the ESI.†

$$A = -\log\left(\frac{T}{1-R}\right) \quad (1)$$

The measured T and R spectra are shown in Fig. S3 (ESI†), and the calculated absorbance spectra of all the as-deposited and HT samples prepared by ALD, SPD, and IBS methods are presented in Fig. 1a. The as-deposited samples are shown *via* dotted lines while the HT samples are shown by solid lines.

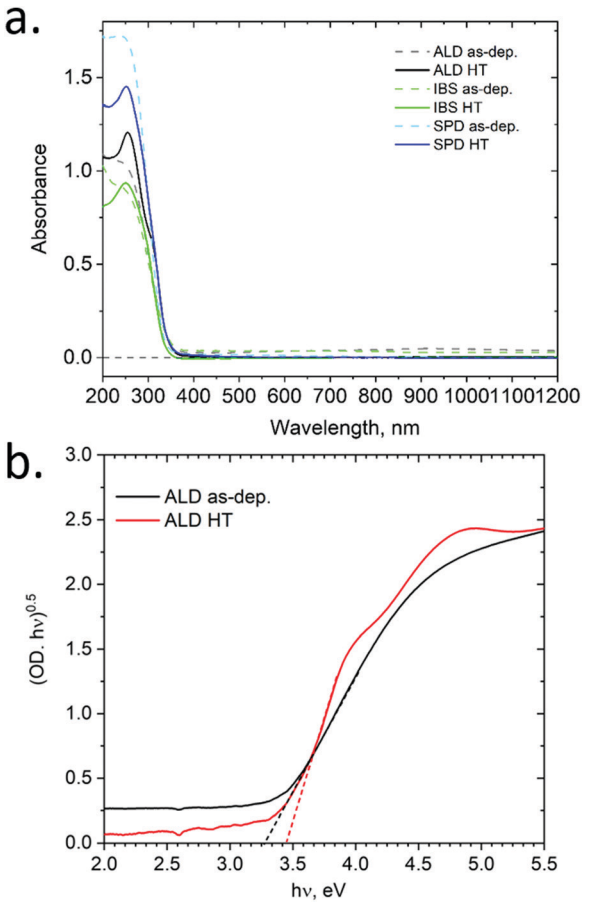

Fig. 1 (a) Reflectance corrected steady state absorbance spectra of samples deposited by ALD, IBS and SPD methods. The inset shows the magnified spectra in the band gap region showing steeper absorption edge after heat-treatment, and (b) Tauc plot presentation of ALD as-dep. and HT TiO_2 spectra.

The spectra reveal that all the samples have a sharp decrease in absorbance after the band gap region. However, the as-deposited ALD and IBS samples show some absorbance in the visible region as well. This is often assigned to the Ti^{3+} state, which is the most pronounced in the case of black TiO_2 fabricated by ALD at a higher growth temperature of 200 °C.[23] A band-like absorption can be seen for all the heat-treated samples at 265 nm together with a minor absorbance shoulder during the absorption decrease at 320 nm; both these features are characteristics of anatase TiO_2.[20] The Tauc plots of ALD samples are presented in Fig. 1b while those for IBS and SPD samples are presented in Fig. S5 (ESI†). The band gaps of all the samples are listed in Table 1. The band gap energy of anatase TiO_2 in the case of thin films is 3.4 eV.[24] This is in agreement with the band gap of our HT thin films which show a band gap of approx. 3.4 eV.

3.2 AFM results

High resolution AFM images were taken to analyze the difference between as-dep. and HT samples deposited by ALD, IBS

Table 1 Band gap of samples deposited by ALD, IBS and SPD methods

Samples	Band gap (eV)
ALD as-dep.	3.32
ALD HT	3.43
IBS as-dep.	3.33
IBS HT	3.49
SPD as-dep.	3.48
SPD HT	3.40

and SPD techniques. The height and phase images of the samples were taken in a few areas of 2 × 2 μm^2 size. Phase images are shown in Fig. 2 to display the fine contrast in grain boundaries for all the samples. All as-deposited samples show no grain boundaries which is a character of amorphous materials. However, for HT samples, the grain boundaries can be seen clearly which depicts the crystalline nature of thin films. The ALD HT sample shows the presence of few small grains (approx. 75–100 nm) which are present over larger grains (>300 nm). For the IBS HT sample, a fine TiO_2 layer with very large grains, >800 nm, is observed. For the SPD HT sample, small grains ranging from 10–50 nm are observed.

The height contrast AFM images of the samples are presented in Fig. S1 (ESI†) along with their roughness values, where the roughness values are found to increase with heat-treatment for all the methods. To analyze the characteristic microstructure of SPD TiO_2 formed by spray droplets, large scale 40 × 40 μm^2 AFM images were taken as shown in Fig. S2a (ESI†). The results show that the thin film consists of circular islands with a diameter of 30–100 μm and a step height of 4–6 nm. In Fig. S1c and f (ESI†), the roughness values were analyzed for individual islands. However, no such large-scale inhomogeneity was found for ALD and IBS TiO_2 thin films.

3.3 XRD results

GIXRD was employed to study the crystal structure of TiO_2 thin films deposited by ALD, IBS and SPD techniques. All the as-deposited samples show amorphous character since no obvious peaks were observed in their GIXRD pattern as shown in Fig. 3. However, all the heat-treated samples showed crystalline nature. A strong diffraction peak at 25.4° is observed for all the HT samples which is characteristic of the anatase TiO_2 phase and it corresponds to the (101) crystal plane (*c*-axis) of TiO_2. In addition, for ALD and SPD HT samples, the peaks at 38.5° and 48.10° were observed, corresponding to the (004) (*c*-axis) and (200) (*a*-axis) crystal planes of anatase TiO_2, respectively.[5] The ALD HT sample shows a more pronounced (004) peak compared to the (200) peak, whereas for the IBS HT sample, a clearly visible (004) peak and a suppressed (200) peak are observed. This indicates that the ALD grown film partially favors the formation of the (004) planes (*i.e.*, part of the anatase crystallites would have their *c*-axis closely perpendicular to the sample surface) and the IBS film partly favors the formation of (200) planes (*i.e.*, part of the anatase crystallites would have their *a*-axis closely perpendicular to the sample surface). However, for the SPD film, there seems not to be any preferential orientation between the (004) and (200) planes.

The deviation of peak intensity ratios from powder diffractograms (ICDD card number 98-016-1908 for anatase TiO_2) is an

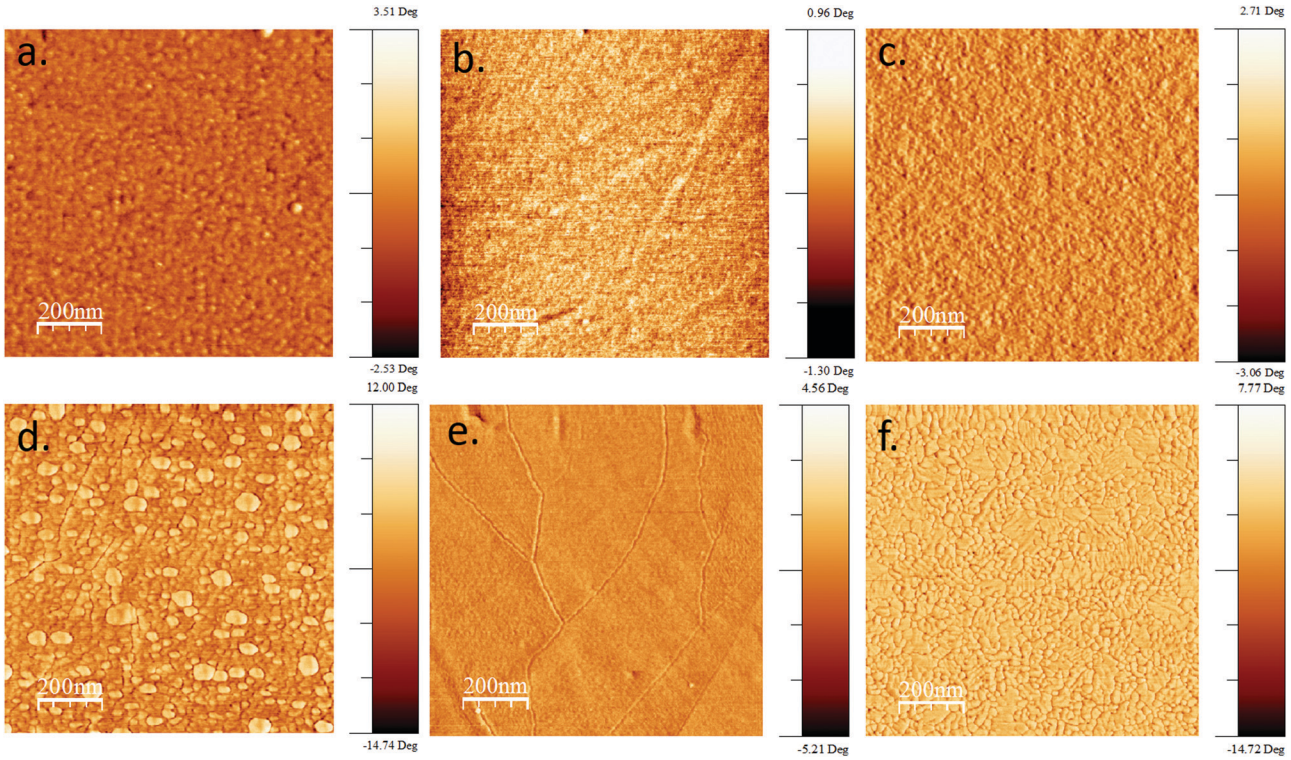

Fig. 2 AFM phase images of as-deposited (a) ALD (b) IBS and (c) SPD samples and heat-treated (d) ALD (e) IBS and (f) SPD samples.

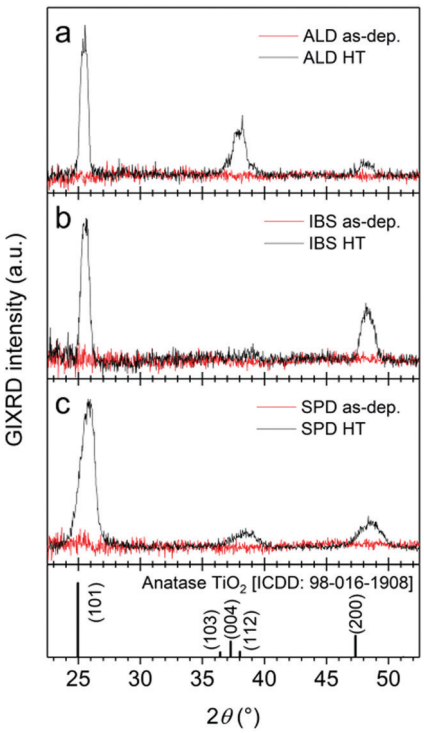

Fig. 3 GIXRD of ALD, IBS and SPD as-deposited and heat-treated samples.

indication of crystal orientation anisotropy, *i.e.* texture.[25] Furthermore, XRD peaks were observed at higher angles compared to the powder diffractograms. This can be caused by stress in TiO_2 thin films which may have resulted from the rapid crystallization upon the heat-treatment. A strong (004) texture has been reported for Nd doped[26] and N doped[27] anatase TiO_2 thin films where dopants have introduced strain in the lattice. For such an unrelaxed TiO_2, the (001) plane has the lowest surface energy, whereas for relaxed TiO_2 the (101) plane is the most favorable surface.[28] Therefore, the reduction of the (004) XRD peak intensity and the high (101) to (004) peak intensity ratio suggests that the IBS TiO_2 HT has a strong (101) plane texture.

A straightforward conclusion from GIXRD measurements is that for all three film deposition techniques the as-deposited TiO_2 films are amorphous, though the exact stoichiometry of the films can be different. The heat treatment finally converts all three samples to anatase type of TiO_2 films with different textures (different orientation of planes).

3.4 Transient absorption spectroscopy

Photo-carrier relaxation dynamics was studied by the pump–probe transient absorption (TA) spectroscopy method in transmittance and reflectance modes. The samples were excited at 320 nm and monitored in two wavelength ranges, 410–740 nm and 840–1050 nm. The results of measurements of the ALD HT sample are shown in Fig. 4 as an example. Apparently, the sample transmittance increases after photo-excitation in the visible range, at $\lambda < 700$ nm. However, the HT TiO_2 does not absorb in the visible part of the spectrum and thus cannot become more transparent. The only feasible explanation for this observation is that the photo-excitation reduces the sample refractive index, and this results in the reduced amount of the light reflected from the sample surface and the increased amount of transmitted light.[29] This is interpreted by the measurement system as a decrease in the sample absorbance. In order to separate the contributions of absorption and refractive index changes to the measured TA responses, the measurements were repeated with the same sample in reflectance mode and the results are presented in Fig. 4b. The results of measurements of other samples can be found in Fig. S8–S12 (ESI†).

4 Data analysis and discussion

4.1 Absorbance and film thickness

The steady state spectra of the samples can be analysed to reveal the film thickness and porosity. The interference of the monitoring light reflected from the front and back film surface results in specific spectral features which depend on the film

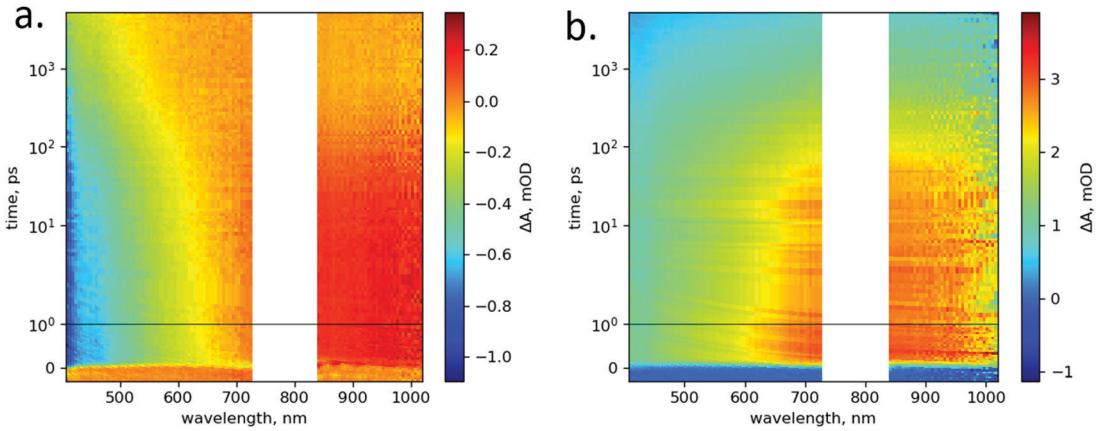

Fig. 4 Transient absorption response of the ALD HT sample measured in (a) transmittance and (b) reflectance modes and presented as 2D maps. The time scale is linear till 1 ps delay time and logarithmic after that. The excitation wavelength is 320 nm.

refractive index and thickness.[30,31] These features are most pronounced when the film thickness is in the order of magnitude of the monitoring wavelength, but can be applied to thinner films, though with lower accuracy. The monitoring light propagation is calculated for the sample structure

$$\text{air}|\text{photo} - \text{activelayer}|\text{substrate}|\text{air} \quad (2)$$

and the transmittance and reflectance of the sample are calculated for known refractive indexes of the film, n_f, and substrate, n_s, and film thickness, d, assuming that the substrate is thick enough to ignore the light interference in the substrate. Here we followed the theoretical framework proposed by Barybin and Shapovalov.[30] To apply the model, we need to know the wavelength dependencies of the refractive indexes of both the film and substrate. A simple single-term Sellmeier equation[32] is used to model the refractive indexes of TiO_2 and quartz substrate (see the ESI† for details). The refractive indices were obtained from Barybin and Shapovalov.[30] The model is complemented by a factor accounting for the possible TiO_2 film porosity, namely the refractive index of the film is presented as[33]

$$n' = (n - 1)p + 1 \quad (3)$$

where n is the refractive index of the bulk material, *e.g.* TiO_2 anatase, n' is the refractive index of the layer with some voids, and the parameter p is in the range $0 < p \leq 1$ where $p = 1$ corresponds to the layer without voids, and smaller p means larger effective volume of voids. Within this approximation, the voids are assumed to be much smaller than the wavelength and homogeneously distributed through the film. Parameter p can also be called the fill factor.

In order for the model to work well in the blue and near UV parts of the spectrum, one also needs to account for the sample absorption. This is especially important for the as-deposited sample when the crystal structures are not well formed and the film has detectable absorption due to a high degree of disorder and large number of defects and trap states. This is accounted for by adding a smoothed step-like absorption extinction coefficient switching from a constant value to zero at the wavelength corresponding to the band gap. The model is described in detail in the ESI† and was applied to fit the measured absorbance spectra of the sample. The blue side of the wavelength range was limited to 330 nm as the single-term Sellmeier refractive index model does not work well at shorter wavelengths. The result of the spectrum fit is presented in Fig. 5 using the examples of ALD as-deposited and HT samples. The fitting results for all samples are summarised in Table 2.

The spectra fit the result in $p \approx 1$ for HT ALD and IBS samples. The calculated thickness $d \approx 30$ nm is in good agreement with the thickness estimated by other methods. This confirms the formation of continuous and homogeneous TiO_2 films in both cases. Also, the spectrum of the as-deposited IBS film is well approximated by the model and gives parameters close to expected (and of the HT sample). However, the thickness calculated for the as-deposited ALD sample, 90.4 nm, deviates significantly from the expectation, 30 nm. An apparent

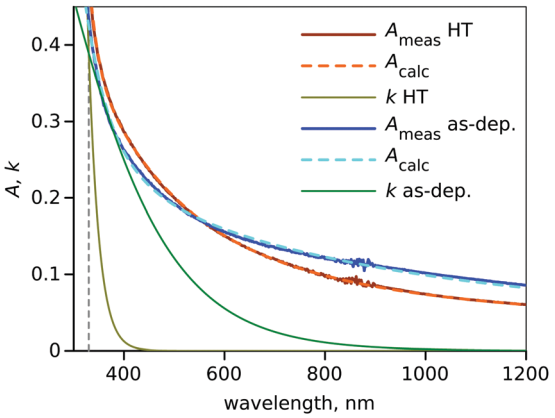

Fig. 5 Measured (A_{meas}) and modelled (A_{calc}) absorption spectra of ALD as-deposited and HT samples. The model uses an approximation for absorption extinction coefficient k, which is also shown for both samples, see text for details.

Table 2 Film thicknesses, d, and porosity parameters, p, estimated from the absorption spectra fits

Sample	d (nm)	p	$d \times p$ (nm)
ALD as-deposited	90.4	0.66	59.4
ALD HT	32.2	0.97	31.1
IBS as-deposited	23.1	1.05	24.3
IBS HT	31.9	0.91	28.9
SPD as-deposited	94.6	0.58	55.2
SPD HT	64.7	0.68	44.3

explanation is that the as-deposited film is porous, and this agrees with $p = 0.66$. The effective thickness can be estimated as $d \times p$ (the thickness without pores) and it is still almost two times larger than expected. The most possible reason for the discrepancy is the incorrect model for the refractive index spectrum of the as-deposited ALD films. Indeed, we used TiO_2 polyxtal[32] as a guess, but we lack actual knowledge of the refractive index.

The values of d and p are definitely the least accurate, as the absorption spectra model presumes uniform film thickness on the lateral scale. This assumption is particularly inaccurate for SPD samples as can be seen from the large scale AFM image presented in Fig. S2 (ESI†). Since the surface thickness is quite inhomogenous, the effective thickness ($d \times p$) of the HT sample is 44.3 nm, which is close to the desired value of 30 nm and agrees with somewhat high absorption of SPD samples (Fig. 1a). This indicates that SPD films retain some porosity even after the heat treatment.

4.2 Transient absorbance spectra calculations

While measuring the TA spectrum of the sample, the probe light reflection takes place from both sides of the TiO_2 film resulting in light interference inside the film, which makes exact calculations of the sample transmittance and reflectance rather complicated.[22] However, if interference can be neglected due to the small sample thickness and/or small reflection at the

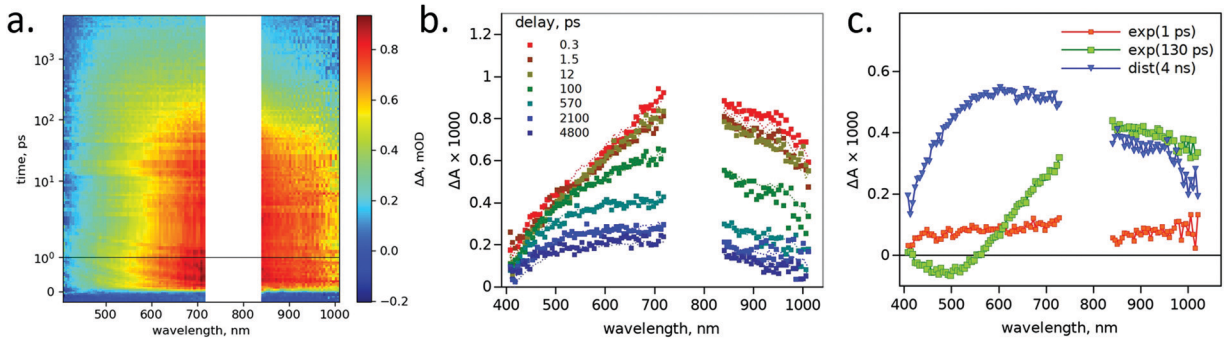

Fig. 6 (a) Calculated ΔA response of the ALD HT sample, (b) time resolved ΔA spectra at different delay times, and (c) decay associated component spectra obtained from these data using the fit model consisting of two exponential (1 and 130 ps) and one distributed decay component (4 ns, see the text for details).

film-substrate interfaces, eqn (1) can be used to calculate the absorbance from transmittance, T, and reflectance, R, spectra of the sample. Within this approximation the photoinduced transient absorbance, ΔA, can be calculated from the measured TA responses in transmittance mode, ΔA_T, reflectance mode, ΔA_R, and the steady state reflectance spectrum, R, of the sample as (for details see the ESI;† transient absorption (TA) measurements in transmittance and reflectance modes – estimation of the photoinduced absorbance change)

$$\Delta A = -\log\left[\frac{(1-R)10^{-\Delta A_T}}{1-R10^{-\Delta A_R}}\right] \quad (4)$$

The results of the calculations are presented in Fig. 6a for the ALD HT sample as an example. The calculated change in absorbance is positive through the whole studied wavelength range and delay times as expected. These data can be analyzed in a standard manner to investigate the type of carrier generating the TA response. We have used a global fit of the data and adjusted the fit model to minimize the number of components but not compromising the fit goodness and obtaining random residuals (see the ESI† for details of trials with different fit models). For all HT samples, the same model consisting of two exponential and one distributed decay components was adequate, which simplified sample comparison. The results for the fit of the ALD HT sample are presented in Fig. 6c as an example and for the other samples, the fits are shown in the ESI.† Though three components were used, the fast decay component (1 ps) is relatively weak and probably can be attributed to the thermal relaxation of the photo-carriers in the conduction band and it is non-essential for this study. Two decay associated components to pay attention to are, the 130 ps exponent and the long-lived distributed decay. The spectrum associated with the 130 ps (exponential) time constant shows the spectrum shape transformation with an absorbance decay in the 600–1000 nm range and some increase at shorter wavelengths. The final relaxation is essentially non-exponential but can be well approximated by distributed decay with a central time constant of 4 ns and a relative distribution width of 13 (see the ESI† for the model description).

By ignoring the fast (<1 ps) and relatively weak TA signals at the beginning, the absorbance change of all HT samples follows the same pattern: (1) the initially formed state has a broad-band absorption with a flat maximum in the range of 600–900 nm, which can be seen as the time resolved TA spectrum at 12 ps delay in Fig. 6b; (2) this is followed by the blue-shift of the absorption maximum to the 500–700 nm region with the time constant in the range of 50–130 ps (see Table 2), which can be seen at a longer delay time, *e.g.* at 2100 ps in Fig. 6b, and this is the spectrum of the long-lived distributed decay component.

The transient absorbance of the as-deposited samples is also broad-band and decays non-exponentially, but there is no visible change in the spectrum shape during the decay and from the very beginning (right after excitation) the broad absorption maximum is located in the visible part of the spectrum, 600–700 nm.

A comparison of the photo-carrier recombination dynamics in different samples is presented in Fig. 7 by plotting ΔA time profiles close to the maximum of the long-lived component. The decay plots for the HT samples are taken at 600 nm for comparison and are fitted by exponential and distributed decay time constants. Apparently, the difference in the lifetimes of the HT samples is rather minor, evidencing similar charge carrier dynamics. We note that the IBS HT sample depicts a bit more shallow decay profile compared to the other samples evidenced by the slightly higher transient absorbance signal for >1000 ps. Also, the lifetime dependence on the thickness of the samples was also studied. A 200 nm thick sample of TiO_2 was prepared by IBS to study the dependence of the charge carrier lifetimes on the sample thickness. It was observed that with the increased thickness of films, the lifetime does not get any better, at least in the nanometer scale range, as shown in Table S2 (ESI†).

The decay profiles of the HT samples are rather similar to those reported by Durrant and co-authors for TiO_2 anatase nanoparticles.[34] They concluded that the nanostructure size has a minor effect on the photo-carrier recombination, and the main relaxation pathway is the bulk recombination. This agrees with our observation showing rather similar relaxation for three

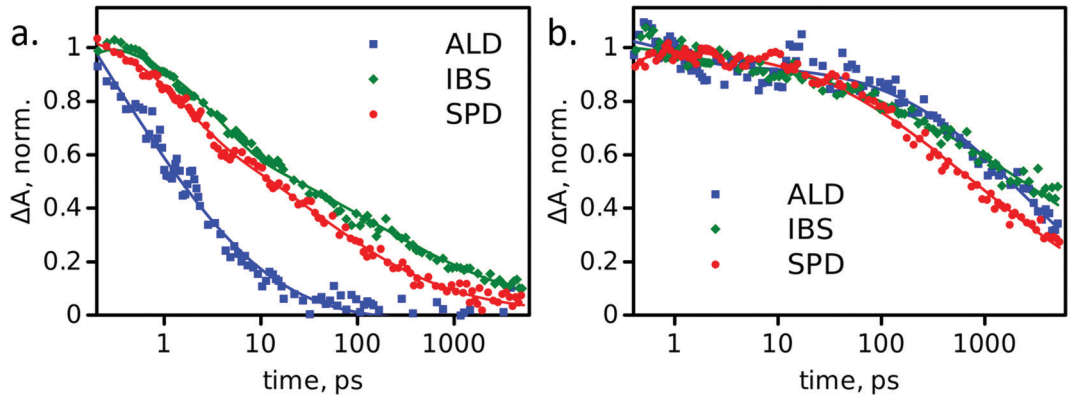

Fig. 7 Normalized ΔA decays in the visible part of the spectrum of the (a) as-deposited ALD, IBS and SPD samples at 670 nm and (b) HT samples at 600 nm.

types of the samples after HT, which have rather different morphologies and different lateral sizes of the crystal domains.

The transient absorbance (ΔA) decay profiles of the as-deposited samples were almost identical at different wavelengths for the same sample but different for different samples. The latter is illustrated in Fig. 7a by presenting decays at 670 nm.

There are a number of theoretical, computational and experimental studies on the intra-band gap states in TiO_2 and its spectral features.[35–37] The broad absorbance band with maximum in the 700–900 nm range was assigned to trapped electrons and the band with maximum in the 450–650 nm range to trapped holes.[35] The free electrons in the conduction band are expected to have slowly increasing absorption toward the longer wavelengths and show no spectral feature in the range of our study (410–1060 nm). There was also an analysis of hole trap states in the bulk and surface states,[38] which predicts the absorption maximum of the bulk hole traps to be in the 600–700 nm range and surface traps at <550 nm. Based on these studies, we can suggest that the absorption observed in a few ps delay time (such as at 12 ps shown in Fig. 6b) is a mixture of absorption spectra of trapped electrons and holes, and shallow trapped electrons, which should have a broad and featureless TA spectrum. Trapping/detrapping of shallow trapped electrons is a slow process and it takes tens of picoseconds (130 ps in the case of the ALD HT sample) to establish an equilibrium of deep trapped electrons and holes. The recombination of the trapped carrier is slow, extended to the nanosecond time domain and most probably it is governed by the thermally activated carriers whose population must be very low in the wide band gap semiconductor such as TiO_2.

This interpretation suggests that there are virtually no free electrons in the conduction band already at picosecond delay time, or the trapping process is fast, <1 ps. This agrees with the recent report of subpicosecond trapping of the photogenerated electrons.[39] However, there must be a significant population of the shallow trapped electrons contributing to the carrier dynamics in the tens of picosecond time scale. However, experimentally, this is observed as a minor increase of the TA in the range of 400–500 nm indicated by a 130 ps component in the case of the ALD HT sample.

The as-deposited samples can be classified as amorphous TiO_2. Although the as-deposited thin films prepared by ALD, IBS and SPD methods have apparently different amorphous nature and the carrier lifetime differs by more than one order in magnitude. The AFM images suggest very different morphologies of the samples prepared by these three methods. It should be noted that different metal–organic Ti precursor compounds and deposition temperatures were used for preparing ALD and SPD samples, whereas IBS used a physical vapor deposition technique without organic precursors that may reside in the thin films.

The ALD deposition temperature was 150 °C while the substrate temperature was 200 °C for SPD samples, which may result in different types of amorphous TiO_2 as-deposited samples. However, at a qualitative level, the TA spectra of all as-deposited samples show broad bands with the maximum in the range of 600–750 nm, or in the same range as the long-lived components of the HT samples shown in Fig. 8. This can be attributed to trapped holes as explained in the case of the ALD HT sample in Fig. 6b. However, the absorption of the SPD HT sample is somewhat lower at the blue side of the

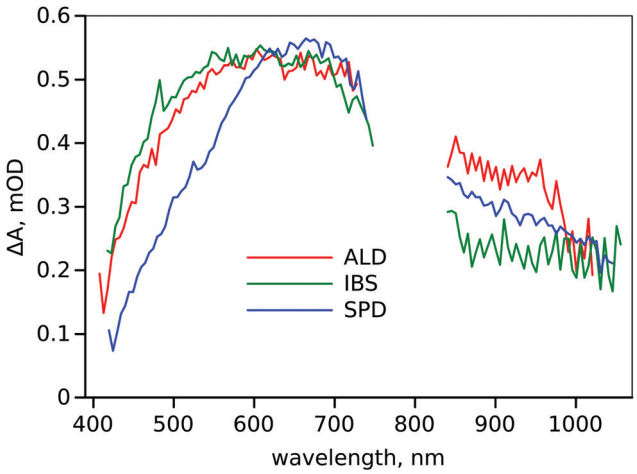

Fig. 8 Decay associated spectra of the long-lived components of the HT samples deposited using ALD, IBS and SPD techniques.

band (<550 nm) which can be due to the different proportions of the bulk and surface trap states.

4.3 Evaluation of photocatalytic performance

To evaluate the photocatalytic activity of TiO_2 thin films, the photodegradation test of methylene blue (MB) was conducted on all the as-dep. and HT thin films deposited *via* ALD, IBS and SPD techniques. MB degradation on a surface is commonly considered to follow the Langmuir–Hinshelwood mechanism in the first order, $c = c_0 \exp(-kt)$, for which the rate constant, k, can be analyzed as the slope of $-\ln(c/c_0)$ *vs.* time curve.[40]

A bare substrate was measured as a control sample (Fig. 9a) to show the magnitude of MB degradation without TiO_2 thin films, for example, due to the MB photolysis. Fig. 9 shows that all the TiO_2 thin films were photocatalytically active compared to the bare substrate which showed a negligible degradation rate of 0.0002 min^{-1}. The degradation performance of all HT thin films improved as compared to that of the as-dep. samples. Also, it was interesting to find that the IBS HT films showed the highest degradation activity with a rate constant of 0.0042 min^{-1} (corresponds to the initial photonic efficiency of 0.0022%) as shown in Fig. 9b. This result is in compliance with our GIXRD and TAS measured data where the IBS HT samples showed the strongest texture and long lifetime of charge carriers. Also, the IBS HT thin films were composed of pure sputtered TiO_2 as compared to HT thin films prepared by ALD and SPD techniques which are chemical vapor deposition processes and may contain some impurities from precursor materials. The catalytic activity of anatase TiO_2 depends on the surface facet orientation. High reactivity facets (001) and (100)/(010) are desired for photocatalytic applications, but have also high surface energies and are therefore more rare.[41,42] However, it should be noted that all the HT samples used for this study are of anatase phase and this phase of TiO_2 is preferred over the rutile phase of TiO_2, since it shows better photocatalytic activity as studied by Wang *et al.*[43] The high-degree of oxide-defects in the as-deposited films resulted in short carrier lifetimes, and therefore, low photocatalytic activity. Also, a strong film texture is particular to physical vapor deposition techniques, such as IBS, and the adjustment of deposition parameters allows for further optimization of texture mediated TiO_2 photocatalytic activity.[44]

4.4 Energy diagram

The band gaps for all the as-deposited and heat-treated samples prepared by ALD, IBS and SPD techniques are listed in Table 3. Assuming the absorption band position of trapped holes to be in the range of 500–700 nm, the energy level of the traps must be in the range of 1.8–2.5 eV over the VB, which agrees with previous experimental and theoretical studies.[35,36] However, in our case this is most probably due to the superposition of the TA bands arising from the hole trap states and the electron trap states.

The estimation of the energy levels of shallow and deep electron traps is more complicated as there is no delay time at which absorption of trapped electrons could be observed. Therefore, we turn our attention to the hundred picosecond component. As discussed above, its most probable origin is the decay of the shallow trapped electron states. The characteristic feature of this component is a broad absorption band extended to the near IR range. The band shows absorption from 800–

Table 3 Time constants arising from global fit of the calculated $\Delta A(\lambda, t)$ data; τ_1 is the exponential decay component, τ_d is the distributed decay time constant and δ is the relative distribution width

Samples	τ_1, ps	τ_d, ps (δ)
ALD as-dep.	—	0.9 (25)
ALD HT	130	3600 (13)
IBS as-dep.	3.3	170 (100)
IBS HT	53	3600 (100)
SPD as-dep.	1.6	50 (32)
SPD HT	98	1400 (42)

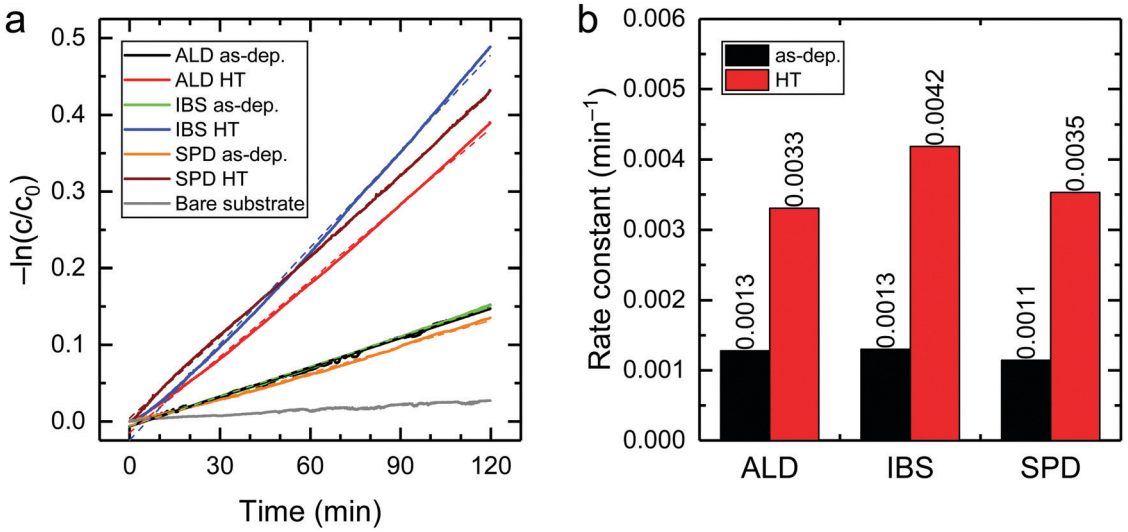

Fig. 9 Photocatalytic degradation of MB under UV irradiation: (a) MB concentration change measured live during UV irradiation and (b) rate constants analyzed as the slope of $-\ln(c/c_0)$ *vs.* time curves. The dashed lines are the linear fits to the data.

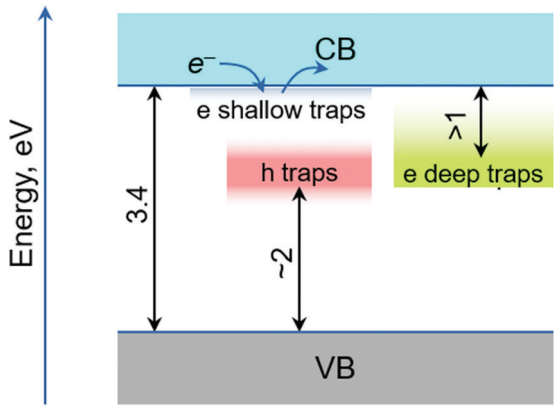

Fig. 10 Tentative energy ranges of the hole (h-traps) and electron (e-traps) traps in the band gap area.

1100 nm but this is differential absorption, meaning that the process associated with it results in lower absorption at wavelengths >600 nm and somewhat higher absorption at shorter wavelengths. This agrees with the interpretation that the electrons at shallow traps can be (thermally) detrapped, and after some traveling, they can again be trapped by deep electron traps. A rough estimation puts electron traps in the range of 1.1–1.5 eV below the CB. It is interesting to note that the relative intensity of the hundred ps component is different for the HT samples prepared by different methods, but the shape is reasonably the same. Also our monitoring range was limited to 1100 nm at the long wavelength side, and most probably the band is extended further to the IR range. It was suggested that the electron trap states start at energies 0.1 eV below the CB.[17] Considering all these, the energy diagram is presented in Fig. 10.

The fast sub-picosecond trapping of the CB carriers generated by photoexcitation was reported[39] and our results are consistent with this observation. One reason for the fast trapping can be rather the high energy of these intra band gap states close to the bottom of the CB. This is observed as the TA band stretched to the IR part of the spectrum.

The TA response of the as-deposited samples is simpler in that there is no change in the spectrum shape and the TA has a non-pronounced band maximum in the 600–700 nm range. Although this band is closer to the expected TA spectrum of trapped holes, most probably there is a mixture of different structural disorders, and oxide defects specific to each deposition method. As a result, the TA spectra and lifetimes of the as-deposited samples are different. Nevertheless, the HT at 500 °C converts all three types of structures to poly-crystalline anatase films with almost similar carrier lifetimes (≈4 ns).

5 Conclusions

Three TiO_2 deposition methods, ALD, IBS, and SPD, were used to prepare films with a nominal thickness of 30 nm. The as-deposited films prepared by all three methods were amorphous in nature. The photogenerated charge carrier lifetimes were different but shorter than 100 ps for all the as-deposited samples. Heat-treatment at 500 °C converted all the amorphous thin films to poly-crystalline anatase TiO_2, albeit with different textures. Also, the AFM study of these samples showed that the morphology and grain size distribution of the films remained dependent on the deposition method. The ALD and IBS techniques resulted in most uniform films, and the SPD technique produced rather inhomogeneous films with their thickness changing in the range of 10–50 nm. Photo-carrier relaxation dynamics was studied using transient absorption (TA) spectroscopy. However, the TA response was affected by both absorption and refractive index changes. The thin film approximation (film thickness is much smaller than the probe wavelength) was used to calculate the TA from pump–probe measurements carried out in transmittance and reflectance modes. The study shows that despite the morphological differences, the carrier lifetimes of the heat-treated samples were virtually independent of the deposition method and extended to a nanosecond time domain (approx. 4 ns). From this point of view, the aim of this study, to hunt for preparing poly-crystalline thin films optimal for photocatalytic activities with longer lifetimes, was achieved in all three cases. As the lifetime of these thin films is independent of the deposition method, all of the above methods can be used for preparing TiO_2 thin film photoelectrodes for photonic applications where a long carrier lifetime is desired and structural homogeneity is not critical. However, in TiO_2 photocatalytic applications, higher activity can be obtained with strongly textured IBS TiO_2 thin films.

Conflicts of interest

There are no conflicts of interest to declare.

Acknowledgements

Ramsha Khan acknowledges the Doctoral program of Tampere University for financial support. We thank Jesse Saari for providing TiO_2 thin films prepared by ALD, Jarno Reuna for providing TiO_2 thin films prepared by IBS, and Maning Liu and Paola Vivo for providing TiO_2 thin films prepared by SPD for the project. This work is part of the Academy of Finland Flagship Programme, Photonics Research and Innovation (PREIN), Decision No. 320165. This work was supported by the Academy of Finland (decision No. 326461).

References

1 Z. Yu, H. Liu, M. Zhu, Y. Li and W. Li, *Small*, 2019, 1903378.
2 T. Moehl, J. Suh, L. Sévery, R. Wick-Joliat and S. D. Tilley, *ACS Appl. Mater. Interface*, 2017, **9**, 43614–43622.
3 M. Khalil, E. S. Anggraeni, T. A. Ivandini and E. Budianto, *Appl. Surf. Sci.*, 2019, **487**, 1376–1384.

4 M. L. de Souza and P. Corio, *Appl. Catal., B*, 2013, **136–137**, 325–333.
5 R. Khan, A. Riaz, M. Rabeel, S. Javed, R. Jan and M. A. Akram, *Appl. Nanosci.*, 2019, **9**, 1915–1924.
6 T.-P. Ruoko, K. Kaunisto, M. Bärtsch, J. Pohjola, A. Hiltunen, M. Niederberger, N. V. Tkachenko and H. Lemmetyinen, *J. Phys. Chem. Lett.*, 2015, **6**, 2859–2864.
7 Z. Tong, T. Peng, W. Sun, S. Liu, W. Guo and X.-Z. Zhao, *J. Phys. Chem. C*, 2014, **118**, 16892–16895.
8 A. Khataee and M. Kasiri, *J. Mol. Catal. A: Chem.*, 2010, **328**, 8–26.
9 J. Schneider, M. Matsuoka, M. Takeuchi, J. Zhang, Y. Horiuchi, M. Anpo and D. W. Bahnemann, *Chem. Rev.*, 2014, **114**, 9919–9986.
10 M. Janczarek and E. Kowalska, *Catalysts*, 2017, **7**, 317–333.
11 M. R. Hoffmann, S. T. Martin, W. Choi and D. W. Bahnemann, *Chem. Rev.*, 1995, **95**, 69–96.
12 T. L. Thompson and J. T. Yates, *Chem. Rev.*, 2006, **106**, 4428–4453.
13 R. Qian, H. Zong, J. Schneider, G. Zhou, T. Zhao, Y. Li, J. Yang, D. W. Bahnemann and J. H. Pan, *Catal. Today*, 2019, **335**, 78–90.
14 A. L. Linsebigler, G. Lu and J. T. Yates, *Chem. Rev.*, 1995, **95**, 735–758.
15 M. Kong, Y. Li, X. Chen, T. Tian, P. Fang, F. Zheng and X. Zhao, *J. Am. Chem. Soc.*, 2011, **133**, 16414–16417.
16 E. Wang, W. Yang and Y. Cao, *J. Phys. Chem. C*, 2009, **113**, 20912–20917.
17 A. Yamakata and J. J. M. Vequizo, *J. Photochem. Photobiol., C*, 2019, **40**, 234–243.
18 A. Yamakata, H. Vequizo, J. Jhon and M. Matsunaga, *J. Phys. Chem. C*, 2015, **119**, 24538–24545.
19 S. Hu, M. R. Shaner, J. A. Beardslee, M. Lichterman, B. S. Brunschwig and N. S. Lewis, *Science*, 2014, **344**, 1005–1009.
20 R. Khan, H. Ali-Löytty, J. Saari, M. Valden, A. Tukiainen, K. Lahtonen and N. V. Tkachenko, *Nanomaterials*, 2020, **10**, 1567.
21 Y. Tachibana, K. Umekita, Y. Otsuka and S. Kuwabata, *J. Phys. D: Appl. Phys.*, 2008, **41**, 102002.
22 H. P. Pasanen, P. Vivo, L. Canil, A. Abate and N. Tkachenko, *Phys. Chem. Chem. Phys.*, 2019, **21**, 14663–14670.
23 H. Ali-Löytty, M. Hannula, J. Saari, L. Palmolahti, B. D. Bhuskute, R. Ulkuniemi, T. Nyyssönen, K. Lahtonen and M. Valden, *ACS Appl. Mater. Interfaces*, 2019, **11**, 2758–2762.
24 K. Usha, B. Mondal, D. Sengupta, P. Das, K. Mukherjee and Kumbhakar, *Opt. Mater.*, 2014, **36**, 1070–1075.
25 P. Acevedo-Peña, F. González, G. González and I. González, *Phys. Chem. Chem. Phys.*, 2014, **16**, 26213–26220.
26 A. Ali, E. Yassitepe, I. Ruzybayev, S. Ismat Shah and A. S. Bhatti, *J. Appl. Phys.*, 2012, **112**, 113505.
27 S. Deng, S. W. Verbruggen, S. Lenaerts, J. A. Martens, S. Van den Berghe, K. Devloo-Casier, W. Devulder, J. Dendooven, D. Deduytsche and C. Detavernier, *J. Vac. Sci. Technol., A*, 2014, **32**, 01A123.
28 A. Vittadini, A. Selloni, F. P. Rotzinger and M. Grätzel, *Phys. Rev. Lett.*, 1998, **81**, 2954–2957.
29 Y. M. Evtushenko, S. Romashkin, N. Trofimov and T. Chekhlova, *Phys. Procedia*, 2015, **73**, 100–107.
30 A. Barybin and V. Shapovalov, *Int. J. Opt.*, 2010, 137572.
31 T.-S. Oh, Y. S. Tokpanov, Y. Hao, J. W. C. and S. M. Haile, *J. Appl. Phys.*, 2012, **112**, 103535.
32 R. D. Shannon, R. C. Shannon, O. Medenbach and R. X. Fischer, *J. Phys. Chem. Ref. Data*, 2002, **31**, 931–970.
33 H. A. Santos, *Porous Silicon Biomed. Appl.*, 2014, pp. 507–526.
34 M. Sachs, E. Pastor, A. Kafizas and J. R. Durrant, *J. Phys. Chem. Lett.*, 2016, **7**, 3742–3746.
35 F. Nunzi, F. De Angelis and A. Selloni, *J. Phys. Chem. Lett.*, 2016, **7**, 3597–3602.
36 T. Yoshihara, R. Katoh, A. Furube, Y. Tamaki, M. Murai, K. Hara, S. Murata, H. Arakawa and M. Tachiya, *J. Phys. Chem. B*, 2004, **108**, 3817–3823.
37 R. Katoh, M. Murai and A. Furube, *Chem. Phys. Lett.*, 2010, **500**, 309–312.
38 P. Zawadzki, *J. Phys. Chem. C*, 2013, **117**, 8647–8651.
39 Y. Zhang, D. T. Payne, C. L. Pang, C. Cacho, R. T. Chapman, E. Springate, H. H. Fielding and T. Geoff, *J. Phys. Chem. Lett.*, 2019, **10**, 5265–5270.
40 A. Houas, H. Lachheb, M. Ksibi, E. Elaloui, C. Guillard and J.-M. Herrmann, *Appl. Catal., B*, 2001, **31**, 145–157.
41 H. G. Yang, C. H. Sun, S. Z. Qiao, J. Zou, G. Liu, S. C. Smith, H. M. Cheng and G. Q. Lu, *Nature*, 2008, **453**, 638–641.
42 N. Roy, Y. Sohn and D. Pradhan, *ACS Nano*, 2013, **7**, 2532–2540.
43 X. Wang, A. Kafizas, X. Li, S. J. A. Moniz, P. J. T. Reardon, J. Tang, I. P. Parkin and J. R. Durrant, *JPCC*, 2015, **119**, 10439–10447.
44 O. Lyandres, D. Finkelstein-Shapiro, P. Chakthranont, M. Graham and K. A. Gray, *Chem. Mater.*, 2012, **24**, 3355–3362.

